RESEARCH PAPER

The Estimation of Taylor-Quinney Coefficients Using Small Ring Specimens

W.J. Lavie[1] · J.P. Rouse[1] · C.J. Hyde[1]

Abstract

Background The use of the Taylor-Quinney coefficient for introducing a thermal dissipation term into material models relies on understanding its dependencies. These are usually determined through extensive experimentation, wherein temperature variations are monitored in a test piece during mechanical loading.

Objective This study aims to reduce the cost and time necessary to determining the dependencies of the Taylor-Quinney coefficient by proposing a novel small specimen inverse testing method and demonstrating its use on aluminium alloy 7175.

Methods The method proposed is based on mechanical testing of a novel small ring specimen in parallel with FEA simulations. In the experiments, small rings of 7175-T7351 aluminium alloy, 20 mm in outer diameter, were loaded between two pins for different pin displacement rates (namely 1, 1.5 and 2 mm/s) at room temperature and the local specimen temperature field was monitored using an infra-red thermal camera. Fully coupled thermal-mechanical simulations of the tests were performed using a range of Taylor-Quinney coefficients, and the resulting temperature evolutions compared to the experimental results in order to determine appropriate coefficient values for the material.

Results The method presented shows good repeatability and allows for clear observation of thermal dissipation. Taylor-Quinney values ranging 0.51-0.59 are reported for the 7175 alloy, in line with values reported in the literature for similar alloys. Density, specific heat capacity and thermal conductivity, fundamental thermal material properties necessary for the simulations, are also reported for the alloy.

Conclusions The method detailed shows promise for determining Taylor-Quinney coefficients in a wide range of experimental conditions and is proposed as a cheap and fast alternative to full-scale specimen testing of Taylor-Quinney coefficients. Taylor-Quinney values obtained for 7175 aluminium are shown to be much lower than the value of 0.9 often proposed for materials.

Keywords Small Ring · Taylor-Quinney · Aluminium · 7175 · Inverse method · Infrared thermography · Mechanical dissipation · Plasticity

Introduction

In order to provide a thermodynamic justification for material deformation and damage accumulation models, rigorous experimental methods are required which can inform

✉ J.P. Rouse
James.Rouse@nottingham.ac.uk

W.J. Lavie
William.Lavie@nottingham.ac.uk

C.J. Hyde
Christopher.Hyde@nottingham.ac.uk

1   Gas Turbine and Transmission Research Centre (G2TRC),
    University of Nottingham, Nottingham NG7 2RD, UK

fundamental energy balances. It is well known that in many materials, after yield, an increasingly large fraction of input mechanical energy is dissipated as heat [1–3]. In sufficient circumstances (highly localised, high strain rate loadings, for example) this dissipated energy can be observed as a significant change in temperature. The Taylor-Quinney coefficient may be defined as the ratio of either the energy dissipated as heat during plastic straining to the total plastic work done on the material element, noted β_{int}, or of thermal dissipation power to plastic power, noted β_{diff}, as will be expanded upon in "Defining Taylor-Quinney Coefficients" section. It is the most fundamental material parameter associated with thermoplastic effects, however values are often assumed in the literature without proper experimental justification [4].

In addition to allowing for the more robust thermodynamic formulations of material constitutive equations, representative Taylor-Quinney values (or more aptly, Taylor-Quinney relationships since multiple dependencies have been experimentally demonstrated in the literature, as will be discussed in "Known Dependencies of the Taylor-Quinney Coefficients" section) may be used to evaluate plastic dissipation fractions in sophisticated energetic failure criteria. Examples of this are the work of Daily and Klingbeil in relation to low cycle fatigue crack growth [5] and that of Einav et al. regarding development of a coupled damage-plasticity material model [6]. Taylor-Quinney values are of further interest to the simulation of fast deformation processes such as high-speed machining and ballistics where plasticity-induced heat generation can lead to sizeable changes in material properties [7].

The most common way of determining Taylor-Quinney coefficients is by measuring temperature values on a specimen while it is being deformed plastically. For high loading rate testing, this can for instance be done using split-Hopkinson bars [2–4, 8–10] while for slower rates tensile or torsion tests are well established [3, 10–14]. The widespread use of these two experimental methods and their respective loading rate capabilities has highlighted the dependency of Taylor-Quinney coefficients on strain rate for certain materials such as *alpha*-Titanium [3], stainless steel 301 [2], and pure titanium, tin, iron and copper [10] in addition to a widely known dependency on strain for many materials (see for instance [2, 3, 8, 10, 15, 16]). Recent developments in the determination of Taylor-Quinney coefficients are the use of inverse analysis whereby experimental work is assisted by FEA [13, 14, 17, 18] and the measurement of strain using digital image correlation (DIC) [11, 19–24]. Further review of the literature describing methods of obtaining Taylor-Quinney values and their dependencies is to be found in "Known Dependencies of the Taylor-Quinney Coefficients" section. These test methods are all typically performed on conventional, full-sized specimens, raising the issue of keeping track of large moving specimens (potentially within a heating chamber) while maintaining quality temperature readings.

The novel method presented here for obtaining Taylor-Quinney parameters partially assuages these difficulties by using a miniature ring as testing specimen, thereby reducing the surface areas that need to be tracked and on which temperature needs to be read. The ring shape of the specimen also permits a localisation of stress and of the accompanying temperature change, simplifying temperature readings while allowing a large portion of the specimen to be visible outside of the machine grips. Finally, the small dimensions of the specimen along with its simple design allow it to be manufactured in large batches at low cost and from a wide range of raw materials. Full-scale ring specimens have been used in testing to check for defects in piping [25] and small

scalloped rings have been used to determine transverse tube properties [26]. Hyde and Sun also proposed a small ring test as a high sensitivity method for the study of primary and steady state creep [27]. Large (by small specimen standards) gauge lengths of approximately 50 mm were noted for modest levels of total deformation, however it must be noted that gauge length is a function of total ring deflection. The small ring test has also seen recent application for determining the tensile properties of 7175 aluminium [28]. This paper however relates the first use of this type of specimen for the determination of Taylor-Quinney coefficients. The small ring test set-up is summarised in Fig. 1 where both the undeformed and deformed specimen states are shown and the ring is loaded along the y axis. In such tests, a ring is loaded by two pins (allowing for self alignment and a minimal influence of friction on the specimen response) such that it may elongate. For creep testing, a load P is applied diametrically and deflection of the pins is monitored. For nominally constant load creep tests (equivalent to traditional full sized uniaxial tests) adaptive loading must be implemented to account for the change in reference stress as the ring deflects [29].

The testing method presented in the paper is illustrated by determining Taylor-Quinney values for aluminium alloy 7175-T7351. Due to an attractive combination of (relatively) high strength and low density, the 7000 series of aluminium alloys which includes the 7175-T7351 alloy have numerous naval, aerospace, and military applications [30–32] and have consequently received a great deal of attention in the literature. In the work of Benoit et al., for example, the microstructure of two 7000 series alloys was analysed, in addition to room temperature values of fundamental mechanical response parameters such as yield stress, ultimate tensile strength, elongation at fracture, and fracture initiation energy [30]. The orientation of sample forgings and grain size demonstrated no significant influence on yield stress. For 7175 alloys at room temperature, yield strength values
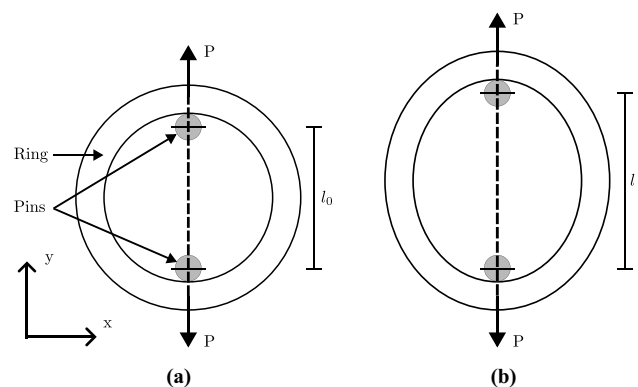
Fig. 1 A schematic of the small ring testing method, showing (**a**) undeformed and (**b**) deformed specimens

of approximately 338 ± 8.5 MPa were determined. Of particular note was the identification of Zn, Mg, and Cu precipitates, which may act as hindrances to dislocation motion (thereby providing an important strengthening mechanism and potentially affecting Taylor-Quinney coefficient values). Zn and Mg precipitates were particularly noted for promoting solution strengthening, precipitate strengthening, and stacking fault strengthening mechanisms. 7175-T735 alloys were also studied in the work of Jaya Rao et al. using nonlinear ultrasonic non-destructive methods [33]. Samples with prior plastic straining were analysed, with resulting nonlinear ultrasonic parameter variations suggesting a two stage dislocation process in the material's deformation behaviour. No Taylor-Quinney values were however found in the literature for this material.

In the present work, tensile small ring tests were performed on 7175 aluminium at room temperature using a constant pin displacement rate while ring temperature was recorded to observe the heating caused by thermoplastic effects. Coupled thermal-mechanical FEA simulations of the tests were performed using an elastic-plastic material model and a range of arbitrary Taylor-Quinney coefficients. Experimental and simulated results were then compared in order to deduce values of β_{int} for the material using an inverse method. It is worth noting that while a 7000 series aluminium alloy is used in the present work due to the industrial potential of these alloys, it is expected that the same technique could be applied to any material for which the representative volume element is smaller than the small ring geometry.

Thermoplastic and Thermoelastic Effects for Moderate Strain Rates

Defining Taylor-Quinney Coefficients

Heat generation associated with material straining has received a good deal of attention in the literature. Particular attention has been paid to the Taylor-Quinney coefficient, the most fundamental parameter associated with thermoplastic effects which is of particularly importance in impact analyses [34]. Rittel has however noted that Taylor-Quinney coefficient values are often simply assumed to be 0.9 in otherwise detailed simulations, despite dependencies on factors such as loading rate being experimentally demonstrable [4]. The Taylor-Quinney coefficient (β) may in fact be defined as a function of powers or of energies. In the first case we will denote it β_{diff} and it can be expressed by equation (1), while in the second case it will be denoted β_{int} and can be expressed by equation (2) [15]. In these relations q_P and w_P are the specific energy dissipated as heat (due to irreversibilities associated with plasticity or damage, for example)

and specific plastic work (total mechanical work minus elastic energy), respectively, while a dot denotes rate terms. Note that lower case terms used in this section relate to specific quantities. It is of course easy to show that the fraction of plastic power stored, η, is related to β_{diff} by $\eta = 1 - \beta_{\text{diff}}$ [35]. A relationship between β_{diff} and β_{int} can be developed as equation (3) [36]. In the present work, values of β_{int} are determined, such that they may at times be referred to as β for simplicity.

$$\beta_{\text{diff}} = \frac{\dot{q}_P}{\dot{w}_P} \tag{1}$$

$$\beta_{\text{int}} = \frac{q_P}{w_P} = \frac{1}{w_P} \int_0^t \beta_{\text{diff}} \, \dot{w}_P \, d\tau \tag{2}$$

$$\beta_{\text{diff}} = \beta_{\text{int}} + \frac{w_P}{\dot{w}_P} \dot{\beta}_{\text{int}} \tag{3}$$

Known Dependencies of the Taylor-Quinney Coefficients

The determination of β_{diff} and β_{int} for polymer materials has received particular attention in the literature. Rittel used split-Hopkinson bars to study the evolution of both forms of the Taylor-Quinney coefficient in polycarbonate at strain rates ranging 5000 - 8000 s^{-1}. It was noted that both β_{diff} and β_{int} are strain and strain-rate dependent and that they evolve differently [15]. Shao et al. considered the glassy polymers polycarbonate (PC) and polymethyl methacrylate (PMMA) and showed, using material models which accounted for strain hardening and softening, that β_{int} can vary between approximately 0.5 and 0.8 (based on plastic strain magnitude and loading rate) [34]. Maurel-Pantel and co-workers investigated semi-crystalline polyamide 66 (PA66) using digital image correlation (DIC) and infra-red imaging techniques (to evaluate total strain and thermal field parameters, respectively) at multiple tensile strain rates, namely 0.1/s, 0.01/s, and 0.001/s [37]. A difference in peak temperature of 15 °C was noted between different loading rate results, with similar observations for shear tests. Constitutive relations used in this work were based on Billon [38]. PA66 was also studied by Benaarbia et al. for low cycle fatigue conditions [39]. Cycle by cycle evaluations of β_{diff} highlighted hot spots in dissipation fields and a range of values (from 0.4 to 0.8) were noted (over approximately 7000 loading cycles).

In metals too the study of plasticity-induced thermal dissipation has attracted attention, in particular due to the importance of heat generation in high strain rate problems such as impact and industrial forming. Split-Hopkinson (or Kolsky) bars have been extensively used to study β_{diff} and β_{int} in experimental studies. Rittel and coworkers for instance

used split-Hopkinson bars to study the dependence of β_{int} on the dynamic loading mode, and potentially large fluctuations were shown to correlate with loading mode for certain materials (e.g. annealed commercially pure Titanium, grade 2) [4]. Similarly, Hodowany and collaborators used both Kolsky bars and a servohydraulic load frame to determine β_{diff} values in 2024 aluminium and alpha-Titanium for strain rates ranging 1 - 3000 s^{-1} [3, 8]. In the aluminium, values of β_{diff} were found to depend on strain but not strain rate and ranged 0.3 - 0.6 while in the Titanium both dependencies were shown and β_{diff} values ranged 0.6 - ($\approx$) 1. In both metals the amount of energy released as heat increased with plastic strain, until β_{diff} was almost 1. Using similar methodology, Vazquez-Fernandez et al. studied the impact of strain history and rate on β_{int} values for austenitic stainless steel 316 and metastable austenitic stainless steel 301 [2]. Results indicated that while Taylor-Quinney factors depended on the level of strain for both metals, only the 316 steel showed strain rate-dependency. Jovic et al. used split-Hopklinson bars to examine Taylor-Quinney values for 304L stainless steel and noted a decrease in β_{int} with increasing strain [16]. A strong dependence of β_{diff} on strain rate was noted in the work of Fekete for 15Ch2MFA (bainitic structure with fine grains) reactor steel, although 08Ch18N10T (austenitic structure with coarse grains) showed negligible levels of loading rate dependency [35]. Multi-phase (Martensite and Austenite) 304 stainless steel materials were analysed by Zaera et al. [40]. This work highlighted that phase transformation mechanisms can release latent heat, leading to experimental observations where β_{diff} or β_{int} take a value greater than unity, an observation also made by Rusinek et al. for β_{diff} in TRIP steel 800 [41]. Polycrystalline aluminium was investigated by Badulescu, with a relationship between β_{diff} and grain orientation suggested [42]. Soares et al. studied β_{diff} and β_{int} in high purity copper, tin, titanium and iron at strain rates ranging 1.25×10^{-4} to 3100 s^{-1} using tensile testing and split-Hopkinson bars and showed high strain and strain rate dependency in all materials [10]. Varga and Kingstedt studied the influence of microstructure on measured β_{int} in laser powder bed fusion manufactured and wrought Inconel 718 using tension split-Hopkinson bars at a strain rate of 360 s^{-1} [7]. They reported that in this metal initial dislocation density and γ' and γ'' hardening had little influence on measured β_{int} values while a dependence on grain size was observed.

Thermomechanical Modelling

It is worth noting here (in order to assist discussion later in the present work) that the measurement of small temperature changes on the surface of components/specimens has been used for many years to evaluate stress fields in elastic loading cases. Such techniques generally known as thermoelastic stress analysis methods exploit the coupling between stress and temperature and commonly require that material samples are cycled at such a rate that conduction can be neglected [43]. A general expression for the temperature change associated with thermoelastic mechanisms is given in equation (4), where T is the observed temperature, ρ is the material density, C_ϵ is the specific heat capacity at constant strain, σ_{ij} is a component of the symmetric stress tensor, ϵ_{ij} is a component of the symmetric total strain tensor, and Q is an input heat. Since temperature is measured at the surface and adiabatic conditions are assumed, the temperature changes measured are related to surface stresses so that plane stress conditions can be assumed [43]. Furthermore, if conduction is neglected and it is reasonable to consider parameters such as Young's modulus and Poisson's ratio (E and ν, respectively) independent of temperature, equation (4) may be simplified and rearranged to give equation (5), which can relate measured temperature fluctuations to stress state. Note that C_ϵ may be related to the specific heat capacity at constant pressure (C_P) by equation (6) (where α is the coefficient of thermal expansion) and that $\alpha/\rho C_P$ is often referred to as the thermoelastic constant. Thermodynamic justification for thermoelastic effects (and importantly equation (4)) is based on the assumption of reversibility in elastic deformation [44]. The Helmholtz free energy (ψ) may be defined as the internal energy (u, a function of temperature and total strain) minus the product of temperature (T) and entropy (s), or $\psi = u - Ts$. Recalling the first and second laws of thermodynamics and evaluating specific heat and work contributions, an expression for the increment in entropy may be found such that equation (4) can be derived [44].

$$\Delta T = \frac{T}{\rho C_\epsilon} \Sigma \frac{\partial \sigma_{ij}}{\partial T} \epsilon_{ij} + \frac{Q}{\rho C_\epsilon} \text{ for } i, j = 1, 2, 3 \tag{4}$$

$$\Delta T = -\frac{\alpha}{\rho C_P} T \sum_{i=1,2} \sigma_{ii} \tag{5}$$

$$C_\epsilon = C_P - \frac{2E\alpha^2 T}{\rho(1-\nu)} \tag{6}$$

In irreversible processes, such as plastic deformation, there is always an increase in entropy [44]. The definition of Helmholtz free energy presented above ($\psi = u - Ts$) is still valid, however it is important to note that in the elastic-plastic case internal energy is a function of state variables related to, for example, kinematic and isotropic hardening (allowing for the quantification of plastic strain) in addition to the elastic strain component and temperature

(as was assumed in the thermoelastic case). The Clausius-Duhem inequality expresses the second law of thermodynamics in a way which is convenient for continuum mechanics study and may be represented by equation (7), where $\dot{\sigma}$ and $\dot{\epsilon}$ are the stress and strain rate tensors, respectively, and $\dot{q}$ is a heat flux. Equation (7) quantifies a total dissipation d which may be decomposed into an intrinsic component δ_{in} and a thermal conduction component δ_{th} such that $d = \delta_{in} + \delta_{th}$ [39, 45, 46]. Expressions for the two are given respectively in equations (8) and (9). Note that the former is related to variations in internal variables reflecting a change in the material's microstructure and the latter is related to the existence of a temperature gradient across the material. In order to experimentally evaluate δ_{in} ($= \dot{q}_P$) the heat equation must be solved (equation (10), where κ is the thermal conductivity). The thermomechanical coupling contributions $\dot{w}_{tmc}$ included in the heat equation have been neglected in some studies [39], however evaluation may be related in some cases to thermoelastic power [17].

$$d = -\dot{\psi} - s\dot{T} + \frac{1}{\rho}\sigma : \dot{\epsilon} - \dot{q}\frac{\nabla T}{\rho T} \geq 0 \qquad (7)$$

$$\delta_{in} = \frac{1}{\rho}\sigma : \dot{\epsilon} - \dot{\psi} - s\dot{T} \qquad (8)$$

$$\delta_{th} = -\dot{q}\frac{\nabla T}{\rho T} \qquad (9)$$

$$C_P\frac{\partial T}{\partial t} - \frac{1}{\rho}\nabla.(\kappa\nabla T) = \dot{q}_P + \dot{w}_{tmc} \qquad (10)$$

Multiple excellent review articles have been published on thermoplastic effects from both theoretical and experimental perspectives. Interested readers are directed to the work of Bertram and Krawietz [46], Knysh and Korkolis [36], Einav et al. [6], and Pottier et al. [17].

Experimental Setup

The purpose of the small ring testing was to pull rings apart at different rates while monitoring the temperature changes that accompany plastic deformation. Tests were completed using an Instron 8862 test frame (see Fig. 2) and the ring specimens had the dimensions given in Fig. 3. In this set-up, load was transferred from the machine end grips to the small ring sample through Nimonic 80A loading fixtures. The fixtures were button-ended, fixed to the machine using hydraulic collet grips and transmitted load to the ring through Nimonic 80A loading pins. In order to ensure the integrity of the fixtures for investigations in materials of all
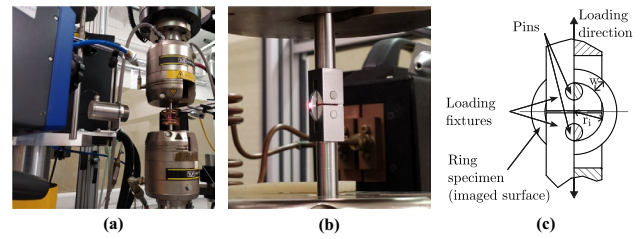
Fig. 2 Experimental set-up used to measure plasticity-driven temperature change showing (**a**) the positioning of the rings and camera, (**b**) a close up view of the small ring within the loading fixtures, and (**c**) a detail drawing of the ring in its mounted position with a partial cut

stiffnesses, the fixtures were made robust with thick cross-sections. This had the effect of obscuring part of the ring but left a sufficient area visible for the analysis presented here. The ring shown in Fig. 2 was not prepared for thermal imaging and is shown for representation purposes only. The induction coil visible in the figure was not used for the work presented in this article.

The tests were run in displacement control using cross-head position to approximate pin displacement. The Young's modulus of Nimonic is approximately three times greater than that of 7175 aluminium and the ring structure of the specimens gave them high flexibility compared to the fixtures. As a result, for a pin load of 2 kN, the upper end of the rupture load of the rings, pin displacements measured were around 1.5 mm of which a strength of materials computation suggests less than 1 % can be attributed to the deformation of the set-up. The machine, fixtures and pins were thus considered to deform very little and cross-head and pin displacements were assumed to be approximately equal. Three pin loading rates (namely 1, 1.5 and 2 mm/s) were applied in order to reveal any rate dependencies for the 7175 aluminium and alter the time scales for heat transfer. Considering an equivalent gauge length of 40 mm for the specimens [27], these displacement rates can be associated

All dimensions in mm
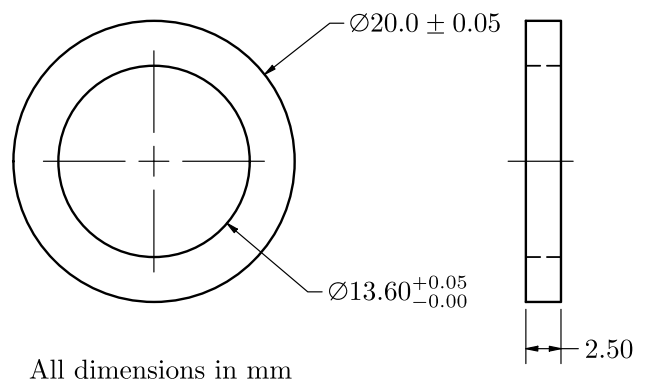
Fig. 3 Dimensions of the small ring specimens

with equivalent strain rates of roughly 2.5, 3.8 and 5 %, respectively. These equivalent rates are given for reference only and do not reflect a physical quantity within the sample. Two tests were run per loading rate for a total of 6 tests.

Temperature fields on the rings were monitored using a FLIR SC7000 series infra-red (IR) thermal camera. They were read on the flat front surface of the rings, as shown in Fig. 2, and sampled at 250 Hz. In order to increase the quality of temperature measurements, the imaged surfaces were lightly abraded using grits P240 to P4000 (abrasive particles of sizes 60 and 5 μm respectively) before applying a light coating of matte black PlastiKote paint.

To determine a value of emissivity for the ring's coated surface and calibrate the camera, thermocouple readings of the atmosphere surrounding a ring were compared to temperatures measured by the camera on the ring assuming an emissivity of 1. Using this method, an emissivity of over 0.99 was determined for the treated surface at room temperature. For a real temperature change of 2 K, the difference measured by the camera without correcting for emissivity is then over 1.995 K so that the error linked to ignoring emissivity correction is around 0.3 %. Considering the low impact of correction, it was assumed in the foregoing that the treated surface has a perfect emissivity of 1.

Heat Exchange Characterisation

In order to investigate thermoplastic effects and estimate Taylor-Quinney coefficients, it is necessary to solve the heat equation (equation (10)). Thermal source terms related to plastic straining must be considered alongside losses to the testing environment (by natural convection, for example) in order to approximate the dynamic temperature field. To this end, some fundamental material properties of 7175-T7351 aluminium need to be determined, namely specific heat capacity, thermal conductivity and density (see equation (10)). Another necessary precondition to solving the heat equation is a characterisation of the heat loss mechanisms. Fundamental thermal properties of 7175-T7351 aluminium were therefore explored and are presented here in a first section while a second section deals with the heat transfers between the ring and its surroundings. Temperature dependence of the thermal properties of interest was ignored due to the very limited scale of temperature variation observed during testing (< 3 K).

Thermal Parameter Determination

Specific heat capacity for 7175 aluminium was estimated using a Netzsch DSC 204 HP Differential Scanning Calorimeter. Tests were performed at ambient conditions. Variations in specific heat capacity were observed over a 5 hour period in order to determine the stability of the results.
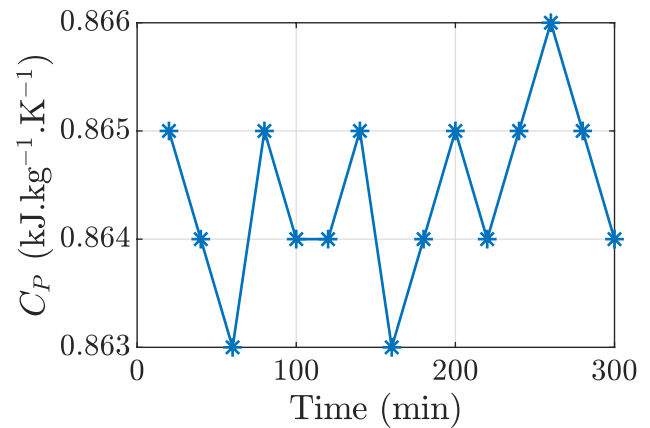

Fig. 4 Variations in specific heat capacity (C_P) recorded over 5 hours

The data obtained is presented in Fig. 4 and shows only minor variations over the sampling period. A mean value of 864.40 J.kg^{-1}.K^{-1} will be used in the following analyses.

The Wiedemann-Franz law is used in the present work in order to estimate thermal conductivity based on electrical conductivity measurements. It may be expressed in the form shown in equation (11), where κ is thermal conductivity, σ_E is electrical conductivity, T is instantaneous temperature (here assumed to be 293 K, representative of typical laboratory ambient temperatures), and L is the Lorenz number (here taken to be 2.44×10^{-8} W.Ω.K^{-2}) [47]. Four point direct current potential drop tests were performed using 4 injection current levels on a 0.03 m $\times$ 0.072 m $\times$ 0.6 m bar of the 7175 aluminium. Results are presented in Table 1. Difficulties in reading small potential drops are suggested for the apparent dependency of thermal conductivity on injection current observed in Table 1, therefore a value of 190.04 W. m^{-1}.K^{-1} is recommended here (being the average of the "stabilised" 2.5 A and 3 A results).

$$\frac{\kappa}{\sigma_E} = LT \tag{11}$$

Density for the 7175 aluminium was estimated using a MicroMetrics Accupyc 1330 pycnometer. 10 successive runs (purges) were performed on a 19.1867 g sample. A mean density value of 2.7581 g.cm^{-3} was found, with a peak deviation from mean of 0.0487 %.

Heat Loss To The Surroundings

In the experimental set-up, the only solid bodies in contact with the ring were the two Nimonic pins. Since Nimonic 80A has a thermal conductivity of around 11.2 W.m^{-1}.K^{-1} or around 6 % of that of 7175 aluminium [48] and the surface of contact was minimal due to the tangential nature of contact, heat transfer between the ring and its surroundings

Table 1 A summary of four point potential drop test results performed on 7175 aluminium and resulting thermal conductivity estimations (based on the Wiedemann-Franz law, see equation (11))

Current (A)	Potential Drop (µV)	Resistance (µΩ)	Electrical Resistivity (Ω.m)	Electrical Conductivity (S.m⁻¹)	Thermal Conductivity (W.m⁻¹.K⁻¹)
1	9.5	9.5	3.42×10^{-8}	29.24×10^{6}	209.04
2	20	10	3.60×10^{-8}	27.78×10^{6}	198.59
2.5	26	10.4	3.74×10^{-8}	26.71×10^{6}	190.95
3	31.5	10.5	3.78×10^{-8}	26.46×10^{6}	189.13

through thermal conduction could be ignored. Similarly, the temperature increase of the rings never exceeded 2 K during testing, making heat transfer through radiation insignificant as it scales with the fourth power of the temperature difference between object and surroundings. On the other hand, the large surface-to-volume ratio of the rings led to comparatively high convective heat fluxes. Heat exchange between the ring and its surroundings was therefore assumed to be dominated by natural convection, such that it could be fully characterised by convective heat transfer coefficients.

Since the temperature of the surroundings was kept constant (within 1 °C) throughout all the tests presented here, heat loss in all tests was characterised by the same convective heat transfer coefficient. A heat transfer coefficient for 7175 aluminium rings was estimated by measuring the temperature of a ring over time as it cooled through natural convection after having been heated by mechanical deformation and having been given time for its temperature field to homogenise through diffusion. Its derivation is detailed in the following paragraphs.

The total heat transfer power for a body of volume V changing temperature at rate $\dot{T}$ is given by equation (12), where ρ and C_P are the density and specific heat capacity, respectively. The convective power is given by equation (13) where A is the convective surface area of the body, h is the heat transfer coefficient, T_s is the surface temperature of the body and T_∞ is the temperature of the surroundings of the body outside of its thermal boundary layer.

$$\dot{Q} = V\rho C_P \dot{T} \tag{12}$$

$$\dot{Q}_{conv} = Ah(T_s - T_\infty) \tag{13}$$

Since heat loss was dominated by convection, then for a ring not undergoing mechanical deformation $\dot{Q} = \dot{Q}_{conv}$. By equating and reworking equations (12) and (13), the heat transfer coefficient can then be expressed as equation (14).

$$h = \frac{V}{A}\rho c_p \frac{\dot{T}}{T_s - T_\infty} \tag{14}$$

The surface area and volume of the ring were respectively 602 mm² and 422 mm³. Before the ring was heated

it was homogeneously at room temperature and its surface temperature was therefore $T_s = T_\infty$. By averaging temperature readings on the ring before it was heated, T_∞ was thus obtained. Two regions of interest (ROIs) of 396 pixels on each side of the loading fixture in the first acquired temperature field frame were averaged, resulting in $T_\infty = 20.09$ °C. Figure 5(a) shows a heatmap of the temperature field in this first frame and the ROIs used for averaging. Since, as explained above, the ring was at room temperature at this point in time, it is hardly discernible from the background. To remedy this, its outline has been highlighted in blue. The coil and thermocouple visible in the frame were not used in the work presented here.

Using the thermal parameters detailed in "Thermal Parameter Determination" section and equation (15), a thermal diffusivity $\alpha = 7.97 \times 10^{-5}$ m².s⁻¹ was determined for 7175 aluminium. Considering the wall thickness w of the ring as characteristic length L_{ch} and using equation (16), a characteristic heat diffusion time τ of 0.129 s was proposed for the rings. For such fast heat diffusion, any gradients in the temperature field caused by localised plasticity were seen to dissipate within seconds of the end of mechanical loading.

$$\alpha = \frac{\kappa}{\rho C_P} \tag{15}$$

$$\tau = \frac{L_{ch}^2}{\alpha} \tag{16}$$
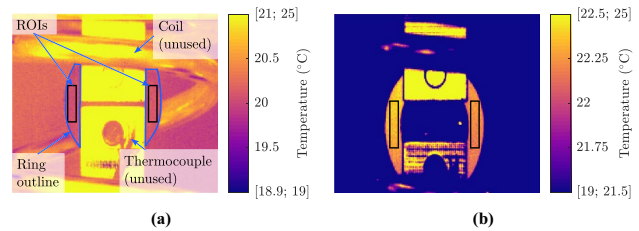
Fig. 5 Heatmaps of temperature on the ring (**a**) before and (**b**) after testing. The regions of interest used for temperature averaging are outlined in black

By taking two IR measurement frames at instants $t_1 < t_2$ over a second after mechanical deformation had stopped, any local temperature peaks on the ring's surface had disappeared and a homogeneous temperature field could therefore be measured on the ring. Homogeneous cooling of the ring could then be observed and $\dot{T}$ was approximated using a first order forward finite difference scheme. The first frame was taken 3 s after the end of loading and was separated from the second frame by 1.684 s. ROIs of 506 pixels on each side of the ring were used to determine average temperature values at both instants. T_s was taken as the spatial average temperature at $t = t_1$ with a value of 22.27 °C. The average temperature value at $t = t_2$ was 22.03 °C, making the cooling rate $\dot{T} = 0.14$ K/s. Figure 5 shows the heatmap of the temperature field at $t = t_1$ overlaid with the ROIs used for averaging temperature. Using the values given here and Eq. 14, the heat transfer coefficient was found to be 106.5 W. $\text{m}^{-2}.\text{K}^{-1}$, an acceptable value when considering the large surface to volume ratio of the specimens [49].

Simulations

In addition to the experimental work detailed above, fully coupled thermo-mechanical simulations of the experiments were performed to compute the temperature change caused by plastic dissipation for various β_{int} values. The simulations aimed to reproduce experimental conditions and were conducted with pin displacement rates identical to those used in the experimental investigations. For each displacement rate, individual simulations were conducted for Taylor-Quinney coefficients of 0.4, 0.5, 0.6, 0.8 and 0.9. Full coupling of the thermal and mechanical effects was necessary to account for heat production and conduction within the material during loading. The simulations were solved in Abaqus standard using eighth models to take full advantage of the three symmetry planes within the set-up. Geometric non-linearity was taken into account due to bending effects. The model used is shown in Fig. 6 in its undeformed state with boundary conditions.

The material model used was elastic-plastic with time-independent isotropic hardening for simplicity. The data used for the constitutive law was obtained from graph WA.311 of the ASM Atlas [50]. A Young's modulus value of 13.9 GPa was used and the plasticity relation was inputted as an array of 17 stress-plastic strain values. Outside the bounds of behaviour presented in [50], perfect plasticity was assumed by Abaqus. The candidate Taylor-Quinney coefficients were implemented in Abaqus using the **inelastic heat fraction** property, and the density and thermal properties used for the material were those detailed in "Thermal Parameter Determination". Elements used to model the ring
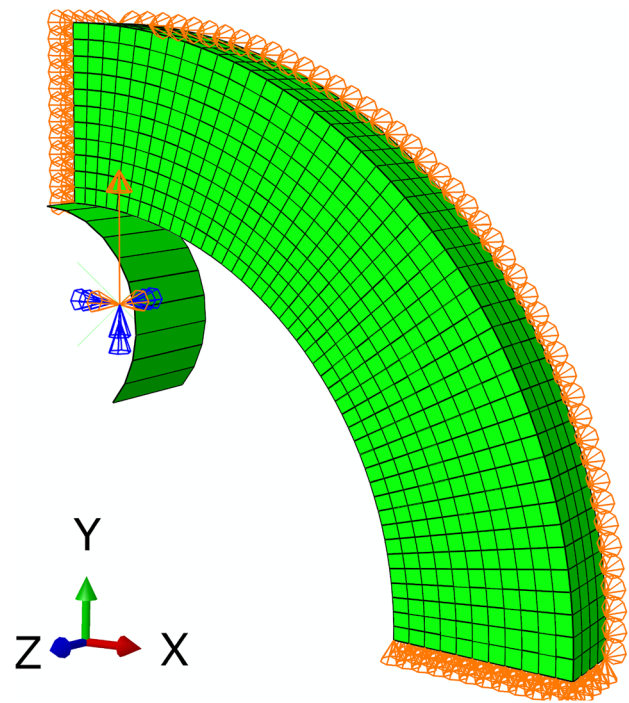

Fig. 6 Simulation set-up

were C3D8T trilinear fully integrated thermally coupled brick elements.

The contact between the ring and pin was modelled as hard, frictionless, and adiabatic due to the low thermal diffusivity of Nimonic 80A and the small contact area with the ring. The pin was modelled as an analytic rigid shell linked to a reference point where all rotations were blocked as well as displacements in the x and z directions shown in Fig. 6. An initial temperature field of 293 K was applied evenly to the part and a convection boundary condition was applied on the outside surfaces using a film condition. The film coefficient used was the heat transfer coefficient determined in "Heat Loss to the Surroundings" section for the experimental configuration. All simulations were led up to a final pin displacement of 1.5 mm (0.75 mm in the model due to symmetry). Loading speed was controlled by setting step durations, affecting thermal transfers but not mechanical behaviour.

Results

Conventional (full size) monotonic testing has suggested minimal time dependency in the constitutive behaviour of AA 7175 at room temperature [28, 51]. Results presented in Fig. 7(a), which show the relationship between pin load and displacement at the strain rates considered here, support this observation for pin displacement rates ranging 1 - 2
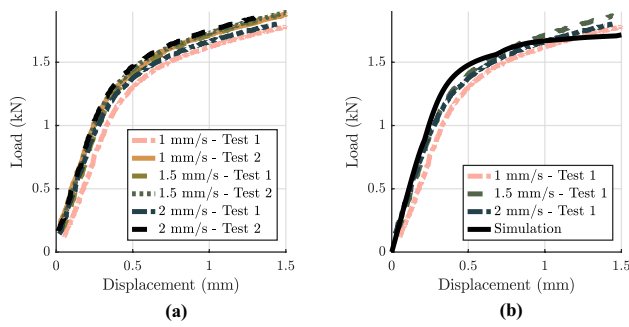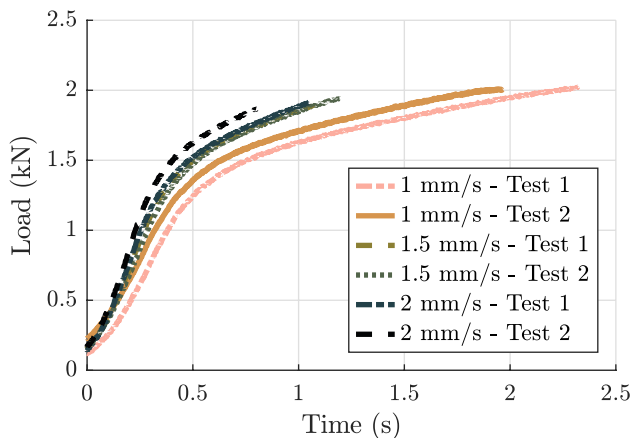
Fig. 7 Pin load/displacement relationships up to 1.5 mm displacement obtained from (**a**) all experiments at the three loading rates (1, 1.5 and 2 mm/s), and (**b**) coupled simulations (with experimental results for comparison)

mm/s. A remarkable level of repeatability should be noted in all observations made here; this directly follows from the self aligning nature of the small ring specimen and the negligible influence of friction on the recorded specimen response [28]. The small differences between curves are largely offsets in displacement values. Indeed, the set-up required pre-loading of specimens by hand leading to pre-load values ranging 10 - 100 N and consequently to differences in reference pin positions. Further evidence of specimen response repeatability can be seen in the time series plots shown in Fig. 8. The data plotted in this figure comes from the same tests as Fig. 7(a) but is shown until rupture.

Figure 7(b) shows the pin force-pin displacement curve computed by the simulations alongside experimental data obtained for all three pin displacement rates. For each pin displacement rate, only the data obtained from the first test is shown to avoid overcrowding the figure. As the material model used in the simulations didn't account for temperature change and wasn't time-dependant, the pin


Fig. 8 Pin load/time relationships until failure observed for loading rates of 1 mm/s, 1.5 mm/s and 2 mm/s

displacement rate had no impact on the force-displacement curve so a single curve is shown for simulated results. The simulation data closely follows the experimental data, suggesting that the simulations were representative of material behaviour and yielded realistic plastic strain values.

The temperature fields obtained from the simulations evolved as expected during loading, with initially homogeneous values giving way to pockets of higher temperature in areas where plasticity was located. The regions with the highest generated temperature were therefore the area of contact with the pins (in the 12 and 6 o'clock positions of the ring, along the loading axis) and the midplane between the pins (3 and 9 o'clock positions). Figure 9b shows the temperature field obtained through simulation at 1.5 mm pin displacement at 2 mm/s and illustrates these features. Since the material model used was not temperature-sensitive, the simulated results for all displacement rates and values of β had this same shape. Experimental temperature fields had a similar shape on the visible regions of the ring, with the 3 and 9 o'clock positions measurably hotter than their surroundings for the higher loading rate of 2 mm/s. The area of the ring in contact with the pins is hidden by the loading fixtures however, obscuring the high temperature variations that occur there. Figure 9(a) shows the temperature field at 1.5mm pin displacement of the first experiment at 2 mm/s. The temperature gradient around the 3 and 9 o'clock positions is evident. It is worth noting here that the fixtures and coil only read as hot because they have different emissivities from the treated copper ring and are in fact at room temperature.

In order to compare experimental and simulated temperature results, a region of interest was chosen over which values were averaged. The ROI was chosen as a line cutting radially through the wall thickness of the ring in the nine o'clock position, as illustrated in Fig. 10(a) for experimental results and Fig. 9(b) for simulation results. Obtaining values along this ROI was straightforward for simulated cases. For experimental results on the other hand, tracking the position of the ROI throughout the test was necessary to keep
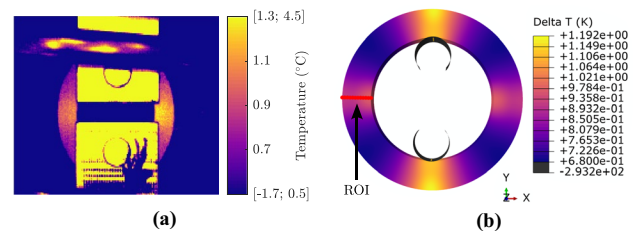

Fig. 9 Relative temperature field on a small ring specimen loaded at 2 mm/s after 1.5 mm pin displacement, (**a**) experimental and (**b**) simulated with $\beta = 0.9$ (mirrored on XY, XZ and YZ planes, with ROI nodes highlighted)
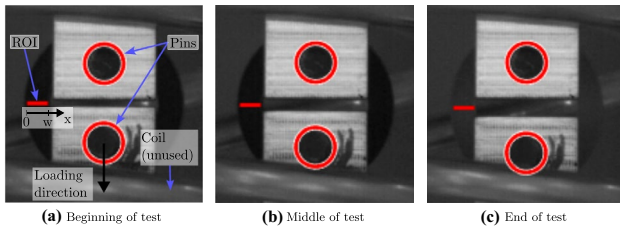
Fig. 10 Detected pin positions and ROI overlaid on levels-of-grey heatmaps for IR data representative of the full test

it static on the ring since the ring moved within the field of view during testing. Bespoke Matlab scripts were developed to automatically detect the position of the ring within IR camera frames. For each frame of data, the script first found the position of the pins using Matlab's *edge* function for Sobel edge detection and deduced the position of the ring's centre as the middle point between the pins. It then found the edges of the ring within a reduced region by using the Sobel method and an initial guess of the edge locations. The pixels closest to the inside and outside edges of the ring were omitted as they tended to overlap with the surroundings, leading to temperature artefacts. Figure 10 shows the positions of pins detected by the script as well as the data points used for temperature sampling at three frames representative of a full test. An induction coil is discernible in the figure but was not used for these experiments. Between the frames shown in Fig. 10(a) and (c), the sampling zone moved by around 4 pixels both horizontally and vertically for a ring wall thickness of around 18 pixels. It is however important to note that, as the ROI was located on a plane of symmetry in the specimen, it was assumed to remain planar.

There were circa 250 to 500 frames per test depending on the displacement rate. By automating the recognition of the ring and the location of the sampling zone, temperature values were extracted consistently from this ROI at every frame. Figure 11 shows the temperature profile across the sampling zone at regular time intervals for each test conducted. Here, the position x is measured from the outside surface of the ring inward and w is the wall thickness, as illustrated in Fig. 10(a). Generally, uniform temperature profiles were observed through the specimen wall thickness, with the average magnitude of these temperature profiles first decreasing with test time due to thermoelastic effects then increasing due to thermal dissipation. For every test the initial temperature drop was smaller than the following increase, with values ranging 0.14–0.18 °C and 0.58–1.7 °C, respectively. Some variation was observed in the temperature values along the profile but no significant features were visible, in keeping with the simulated results. Since the stress and plastic strain fields within the ROI are inhomogenous (the inside edge of the ring sees higher stresses
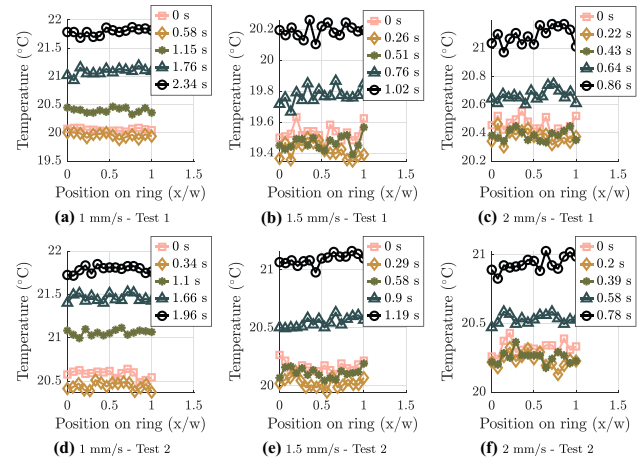
Fig. 11 Temperature profiles in ring at regular time intervals for pin displacement rates of (**a** and **d**) 1 mm/s, (**b** and **e**) 1.5 mm/s, and (**c** and **f**) 2 mm/s

and more plasticity than the outside), this implies that heat generation differences in the ROI due to inhomogeneous plastic deformation were compensated by fast heat diffusion. Testing conditions are therefore not adiabatic, agreeing with the observation that the characteristic diffusion time was short for the experimental time-scales (see "Heat Loss to the Surroundings" section). This interpretation is supported by noting that a Fourier number of 7.8, computed using the formula $F_0 = \alpha t_p / L_{ch}^2$ [52], can be determined for these conditions if a characteristic process time t_p of 1 s is taken. Varga and Kingstedt report that the Fourier number needs to be under 0.01 for a process to be considered adiabatic [7].

The experimental and simulated ROI average temperature changes $\Delta T = T(t) - T(t = 0)$ at time t were then compared to determine β_{int}, denoted β here for ease, values for 7175 aluminium by using an inverse technique. Figure 12(a) shows experimental temperature change - pin displacement curves superposed with simulated ones for the 1.5 mm/s case. The experimental results clearly show an initial thermoelastic temperature reduction followed by a thermoplastic temperature increase, a behaviour also visible in Fig. 11.
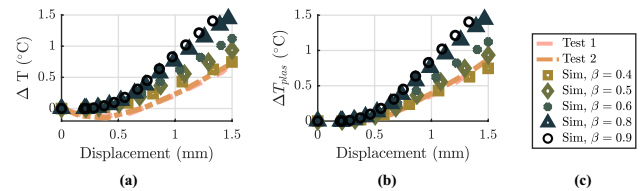
Fig. 12 Experimental and simulated temperature change - displacement curves during testing of a ring at a pin displacement rate of 1.5 mm/s (**a**) before and (**b**) after removing thermoelastic effects, and (**c**) common legend

For displacement rates of 1, 1.5, and 2 mm/s the minimum values of the initial temperature drops averaged over two tests were respectively −0.156, −0.174, and −0.160 K. The simulated results do not show these initial temperature drops because the model used in the simulations accounted only for heat generation caused by plastic deformation and wasn't capable of replicating thermoelastic effects. However, this does not invalidate the model since non-plastic behaviour such as these thermoelastic effects can be ignored in the determination of the Taylor-Quinney coefficient which relates only plastic work and heat dissipation. To better compare experimental and simulated results, the initial thermoelastic cooling was removed from temperature change values. This was done by defining a new temperature change variable ΔT_{plas} with the lowest temperature reached as reference temperature, such that $\Delta T_{plas} = T(t) - \min(T)$. Figure 12(b) shows ΔT_{plas} versus displacement for both experimental and simulated results for a pin displacement rate of 1.5 mm/s.

Experimental results processed in this way for all three testing displacement rates are shown in Fig. 13 together with simulation results for the same pin displacement rates and Taylor-Quinney coefficients ranging 0.4 - 0.9. Generally, simulation and experimental curves can be clearly seen to evolve similarly for all three displacement rates, with initially non-linear behaviour followed by fairly linear behaviour. This shift in behaviour corresponds to the passage within the ROI from elastic to plastic conditions. Indeed since the plastic behaviour of the material is close to perfectly plastic, plastic work and therefore dissipated heat are nearly constant for a given plastic strain increment. As the material within the ROI transitions from elastic to plastic conditions, the heat dissipation per pin displacement increment increases until enough of the ROI is plastic that an

almost linear relationship between heat generation and pin displacement increments is established. Since heat losses by convection and conduction scale linearly with temperature, a near-linear relationship between temperature and displacement increments is also obtained. For both displacement rates of 1 and 1.5 mm/s, the experimental results from the two tests were very similar, suggesting good repeatability of the tests. These results were visually closest to the simulation results obtained for $\beta = 0.4$. This observation is backed up for all four tests by measures of root mean square error (RMSE) which were lowest for Taylor-Quinney values of 0.4 as compared to all others. The RMSE values obtained for pin displacement rates of 1 and 1.5 mm/s and β values of 0.4 thus spanned 2.92e-2–4.97e-2 °C while for other β values RMSE ranged 7.21e-2–5.3e-1 °C with error increasing with β. For the 2 mm/s case, experimental curves for the two tests show different initial non-linear behaviour but match up well in their linear portions. Visually, the simulated curves obtained for Taylor-Quinney coefficients of 0.5 and 0.6 have the closest linear behaviour to the experimental curves in this 2 mm/s case. This observation is confirmed by values of RMSE of 6.16e-2 and 2.83e-2 °C, respectively, for test 1 and $\beta = 0.6$, and test 2 and $\beta = 0.5$.

Discussion

The geometry of the small rings used along with relatively low pin displacement rates allowed for straight-forward detection and tracking of the region of interest for temperature measurements. It is worth noting here that while the displacement rates used were low enough to avoid fast movement of the ROI, they were nonetheless high enough that plasticity-generated heat could be captured by the camera. Temperature changes within the ring were therefore easy to measure with total ranges of over 1.5 K in some tests.

No strong rate dependency in the mechanical behaviour of AA 7175 was observed for loading rates of 1 to 2 mm/s. Note that the rings used here have an equivalent gauge length of around 40 mm [27], implying equivalent strain rates of 2.5 - 5%/s, respectively. Exploration of rate dependency outside this range can be achieved using similar equipment to that detailed here, the limiting parameters being the shutter speed of the camera, the displacement rate achievable by the testing set-up, and, as with all FEA simulations, the capability of the software to resolve fast contact loading. It is also to be expected that by increasing loading rates and consequently reducing time scales over which heat transfer may take place, high local temperature peaks will appear on the ring where plastic strain concentrates. In such a case local temperature changes could potentially be related to local strain rates, allowing for a single experiment to yield Taylor-Quinney coefficients for multiple strain rates. Future work
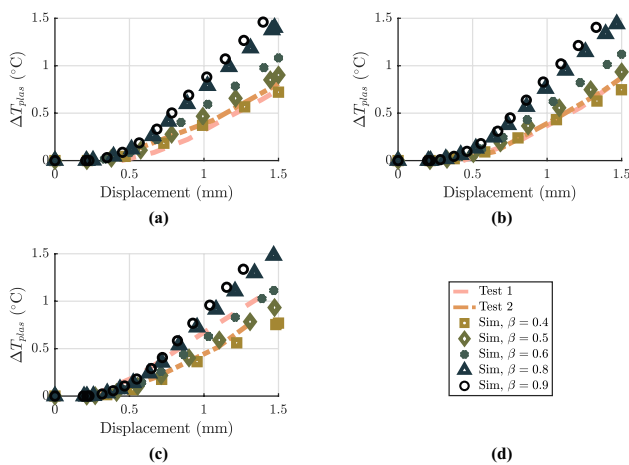

Fig. 13 Experimental and simulated values of average temperature change versus pin displacement for pin displacement rates of (**a**) 1, (**b**) 1.5 and (**c**) 2 mm/s, and (**d**) common legend

could examine the possibilities offered by such testing conditions. Digital image correlation (DIC) could for instance be used to determine local strain rates synchronously with the IR thermography measures, a technique that has seen recent development [11, 19–22]. Alternatively, DIC could be done using infrared thermography imaging directly [23, 24]. Considering the characteristic diffusive time of 0.129 s computed for the ring, displacement rates considerably higher than the ones applied here may need to be used in order to achieve such conditions.

As expected, for the range of displacement rates considered the temperature change in a ring for a given pin displacement increases with loading rate. Using first-order polynomials fitted to the linear sections of the experimental data we can for instance determine that a pin displacement of 1.3 mm results in average temperature increases of 0.58, 0.66, and 0.84 K for displacement rates of 1, 1.5, and 2 mm/s respectively. It is important to note here that all test times were of the order of 2 s and ambient temperature within the room remained stable throughout, such that the entire change in temperature can be ascribed to plasticity-driven heat generation.

Evidence of thermoelastic effects is also clearly discernible in the results presented here. These effects lead to drops in temperature of over 0.1 K and are evident in Figs. 11 and 12(a). They were ignored in the present work as they hold no relation to the Taylor-Quinney coefficient but could be of interest for other applications. The non-cyclic nature of the current tensile pin-loaded small ring test makes further examination of these effects difficult however as relevant conditions have clearly not been achieved. The results discussed here do nonetheless indicate a potential focus for future work, and a small ring cyclic testing method is currently in development at the University of Nottingham that could hold promise in this regard[1]

The temperature - pin displacement curves simulated using arbitrarily chosen Taylor-Quinney coefficients line up well with the experimental results. Since the higher strain portion of the curves pertains unambiguously to plastic behaviour however, further analysis of them can give better approximations of the Taylor-Quinney coefficient. The slopes of the linear portions of all experimental and simulated curves were therefore computed by fitting linear functions to the data using a least-squares optimisation method. As expected the fit is very good for all experimental and simulated curves due to the low levels of hardening shown by AA7175, with 0.9933 and 0.9997 being the lowest R^2 values for experimental and simulated fits, respectively. For each displacement rate, a relationship of the form $dT/du = a\beta + b$
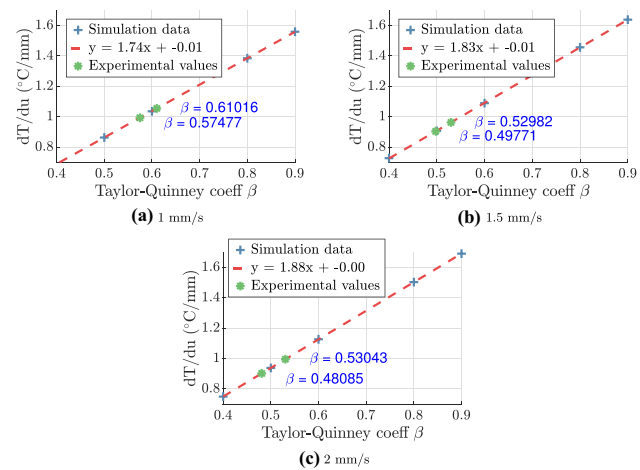
Fig. 14 Deducing Taylor-Quinney coefficients for pin displacement rates of 1, 1.5 and 2 mm/s

can be produced using simulated data. Taylor-Quinney coefficients for each experiment can then be obtained by inputting slopes fitted to experimental data into these relationships. Figure 14 shows the functions obtained using simulation data for all three displacement rates as well as the experimental Taylor-Quinney values obtained. For each displacement rate the Taylor-Quinney coefficient values obtained for the two tests are fairly close together, with relative differences of 6.2%, 6.5%, and 10.3% respectively for the 1, 1.5, and 2 mm/s cases, where the relative difference in a pair of β values is defined as $(\beta_{max} - \beta_{min})/\beta_{min}$. The average Taylor-Quinney values for pin displacement rates of 1, 1.5 and 2 mm/s are 0.59, 0.51, and 0.51, respectively. It will be noted that these values are higher than the ones estimated in "Results" section using the full experimental data. This can be interpreted as an increase in Taylor-Quinney values with increasing strain. Such phenomena have been observed for other materials such as stainless steels 316 and 301 [2], 7075 aluminium [53] and 2024 aluminium [3].

As touched upon previously, for materials with low levels of hardening and in cases where conduction and convection scale linearly with temperature, a linear relationship can be expected between the Taylor-Quinney coefficient and the temperature increase caused by a given pin displacement increment in regions where the material deforms plastically. This is manifestly the case here considering that the linear relations shown in Fig. 14 were all obtained by fitting with an R^2 of almost 1. In such cases it is therefore not strictly necessary to run simulations with more than two Taylor-Quinney values but it allows for a visual estimation of β using graphs such as Fig. 13 for little additional computational cost. For materials which exhibit more pronounced hardening or softening behaviours such linear relationship are not to be expected and more simulations may be needed.

---

[1] PhD thesis to be published shortly by J. Kazakeviciute entitled "Development of a Small Ring Specimen Cyclic Testing Technique"

The relatively low values obtained for the Taylor-Quinney coefficient here have precedent in aluminium alloys, as aluminium alloy 2024 has been shown to have a β_{diff} value of less than 0.4 in some cases [3, 8]. Values of β_{int} of under 0.4 have also been reported by Rittel et al. in both alloys 2024 and 5086 [4], values of 0.4 to 0.7 have been measured for pure aluminium [9], and values of 0.3 to 1 have been reported for alloy 7075 [53].

Conclusions

A small ring tensile testing technique has been employed in order to investigate thermoplastic effects in 7175-T7351 aluminium alloy. Results presented indicate that it is suitable for modest strain rates with potentially rich applications at rates higher than those considered here. The good levels of repeatability shown allied with the small amounts of source material needed have the potential to make small ring tensile tests an effective and efficient means to study some of the various dependencies associated with β. High levels of plasticity have allowed for temperature changes of over to 1 °C to be observed, resulting from intrinsic dissipation. Small specimens hold advantages over full sized equivalents in this field of study in that their small dimensions allow for easy temperature control and measurement. The small ring specimen and testing method presented here hold the further advantages of localising plasticity to a region of the ring while allowing for precise strain measurements thanks to a high effective gauge length. Furthermore, the simplicity of the small ring design and its reduced size make it cheap to manufacture out of small amounts of material. By combining the experimental results with fully-coupled thermal-mechanical Abaqus simulations it was furthermore shown that physically reasonable Taylor-Quinney coefficients ranging 0.48-0.61 could be determined for 7175 aluminium using this set-up. As compared to full sized samples failure is less repeatable (see Fig. 8) however and it is unclear at present how sensitive these results are to tolerances in the specimen design. The isolation of noise in results of this type is a problem that plagues all testing (full sized or small), however the levels of temperature change seen here are large enough that the impact of noise on measured data can be minimised.

Declarations

References

1. Chaboche J-L (1993) Cyclic viscoplastic constitutive equations, Part I: a thermodynamically consistent formulation. J Appl Mech 60(4):813–821. https://doi.org/10.1115/1.2900988. Accessed 3 Dec 2021

2. Vazquez-Fernandez NI, Soares GC, Smith JL, Seidt JD, Isakov M, Gilat A, Kuokkala VT, Hokka M (2019) Adiabatic heating of austenitic stainless steels at different strain rates. J Dyn Behav Mater 5(3):221–229. https://doi.org/10.1007/s40870-019-00204-z. Accessed 20 Feb 2022

3. Hodowany J, Ravichandran G, Rosakis AJ, Rosakis P (2000) Partition of plastic work into heat and stored energy in metals. Exp Mech 40(2):113–123. https://doi.org/10.1007/BF02325036. Accessed 20 Feb 2022

4. Rittel D, Zhang LH, Osovski S (2017) The dependence of the Taylor-Quinney coefficient on the dynamic loading mode. J Mech Phys Solids 107:96–114. https://doi.org/10.1016/j.jmps.2017.06.016. Accessed 3 Dec 2021

5. Daily JS, Klingbeil NW (2004) Plastic dissipation in fatigue crack growth under mixed-mode loading. Int J Fatigue 26:727–738

6. Einav I, Houlsby GT, Nguyen GD (2007) Coupled damage and plasticity models derived from energy and dissipation potentials. Int J Solids Struct 44:2487–2508

7. Varga J, Kingstedt OT (2021) An investigation of the plastic work to heat conversion of wrought and laser powder bed fusion manufactured Inconel 718. Addit Manuf 46:102179. https://doi.org/10.1016/j.addma.2021.102179. Accessed 29 Sept 2022

8. Ravichandran G, Rosakis AJ, Hodowany J, Rosakis P (2002) On the conversion of plastic work into heat during high-rate deformation. AIP Conf Proc 620(1):557–562. https://doi.org/10.1063/1.1483600. Publisher: American Institute of Physics. Accessed 6 Dec 2021

9. Nieto-Fuentes JC, Osovski S, Venkert A, Rittel D (2019) Reassessment of the dynamic thermomechanical conversion in metals. Phys Rev Lett 123(25):255502. https://doi.org/10.1103/PhysRevLett.123.255502. Publisher: American Physical Society. Accessed 20 Feb 2022

10. Soares GC, Hokka M (2021) The Taylor-Quinney coefficients and strain hardening of commercially pure titanium, iron, copper, and tin in high rate compression. Int J Impact Eng 156:103940. https://doi.org/10.1016/j.ijimpeng.2021.103940. Accessed 28 Sept 2022

11. Żaba K, Trzepieciński T, Puchlerska S, Noga P, Balcerzak M (2021) Coupled Thermomechanical Response Measurement of Deformation of Nickel-Based Superalloys Using Full-Field Digital Image Correlation and Infrared Thermography. Materials 14(9):2163. https://doi.org/10.3390/ma14092163. Number: 9

Publisher: Multidisciplinary Digital Publishing Institute. Accessed 6 Dec 2021

12. Macdougall D (2000) Determination of the plastic work converted to heat using radiometry. Exp Mech 40(3):298–306. https://doi.org/10.1007/BF02327503. Accessed 20 Feb 2022

13. Neto DM, Simões VM, Oliveira MC, Alves JL, Laurent H, Oudriss A, Menezes LF (2020) Experimental and numerical analysis of the heat generated by plastic deformation in quasi-static uniaxial tensile tests. Mech Mater 146:103398. https://doi.org/10.1016/j.mechmat.2020.103398. Accessed 20 Feb 2022

14. Pottier T, Toussaint F, Louche H, Vacher P (2011) Experimental estimation of the Inelastic Heat Fraction from thermomechanical observations and inverse analysis. In: Proulx T (ed) Thermomechanics and Infra-Red Imaging, vol 7. Conference Proceedings of the Society for Experimental Mechanics Series. Springer, New York, NY, pp 33–37. https://doi.org/10.1007/978-1-4614-0207-7_5

15. Rittel D (1999) On the conversion of plastic work to heat during high strain rate deformation of glassy polymers. Mech Mater 31:131–139. https://doi.org/10.1016/S0167-6636(98)00063-5

16. Jovic C, Wagner D, Herve P, Gary G, Lazzarotto L (2006) Mechanical behaviour and temperature measurement during dynamic deformation on split Hopkinson bar of 304L stainless steel and 5754 aluminium alloy. Journal de Physique IV (Proceedings) 134:1279–1285. https://doi.org/10.1051/jp4:2006134194. Accessed 30 May 2022

17. Pottier T, Toussaint F, Louche H, Vacher P (2013) Inelastic heat fraction estimation from two successive mechanical and thermal analyses and full-field measurements. Eur J Mech A Solids 38:1–11

18. Dixit US, Raj A, Petrov PA (2022) Determination of temperature distribution in cold forging with the support of inverse analysis. Measurement 187:110270. https://doi.org/10.1016/j.measurement.2021.110270. Accessed 21 Feb 2022

19. Toussaint E, Balandraud X, Le Cam J-B, Grédiac M (2012) Combining displacement, strain, temperature and heat source fields to investigate the thermomechanical response of an elastomeric specimen subjected to large deformations. Polym Testing 31(7):916–925. https://doi.org/10.1016/j.polymertesting.2012.04.013. Accessed 26 Sept 2022

20. Uchida Y, Shiozawa D, Hori M, Kobayashi K, Sakagami T (2022) Advanced technique for thermoelastic stress analysis and dissipation energy evaluation via visible-infrared synchronous measurement. Exp Mech 62(3):459–470. https://doi.org/10.1007/s11340-021-00796-5. Accessed 26 Sept 2022

21. Wang X, Witz J-F, El Bartali A, Jiang C (2016) Infrared thermography coupled with digital image correlation in studying plastic deformation on the mesoscale level. Opt Lasers Eng 86:264–274. https://doi.org/10.1016/j.optlaseng.2016.06.001. Accessed 26 Sept 2022

22. Wang W, Fruehmann RK, Dulieu-Barton JM (2015) Application of digital image correlation to address complex motions in thermoelastic stress analysis. Strain 51(5):405–418. https://doi.org/10.1111/str.12151. eprint: https://onlinelibrary.wiley.com/doi/pdf/10.1111/str.12151. Accessed 26 Sept 2022

23. Wang XG, Liu CH, Jiang C (2017) Simultaneous assessment of Lagrangian strain and temperature fields by improved IR-DIC strategy. Opt Lasers Eng 94:17–26. https://doi.org/10.1016/j.optlaseng.2017.02.012. Accessed 26 Sept 2022

24. Maynadier A, Poncelet M, Lavernhe-Taillard K, Roux S (2012) One-shot measurement of thermal and kinematic fields: InfraRed Image Correlation (IRIC). Exp Mech 52(3):241–255. https://doi.org/10.1007/s11340-011-9483-2. Accessed 26 Sept 2022

25. International Organization for Standardization (1986) Metallic materials - Tube - Ring tensile test. Standard ISO 8496:1986. International Organization for Standardization

26. Arsene S, Bai J (1996) A new approach to measuring transverse properties of structural tubing by a ring test. J Test Eval 24(6):386. https://doi.org/10.1520/JTE11461J. Accessed 22 Sept 2022

27. Hyde TH, Sun W (2009) A novel, high-sensitivity, small specimen creep test. J Strain Anal Eng Des 44(3):171–185. https://doi.org/10.1243/03093247JSA502

28. Kazakeviciute J, Rouse JP, Focatiis DSA, Hyde CJ (2019) The development of a novel technique for small ring specimen tensile testing. Theoret Appl Fract Mech 99:131–139. https://doi.org/10.1016/j.tafmec.2018.11.016

29. Hyde CJ, Hyde TH, Sun W (2017) Small ring testing of high temperature materials. Key Eng Mater 734:168–175

30. Benoit SG, Chalivendra VB, Rice MA, Doleski RF (2016) Characterization of the microstructure, fracture, and mechanical properties of aluminum alloys 7085-O and 7175–T7452 hollow cylinder extrusions. Metall and Mater Trans A 47(9):4476–4483. https://doi.org/10.1007/s11661-016-3624-2

31. Wen J, Fan Y, Wang G, Jin L, Li X, Li Z, Zhang Y, Xiong B (2016) Aging behavior and precipitate characterization of a high Zn-containing Al-Zn-Mg-Cu alloy with various tempers. Mater Des 101:16–23

32. Goueffon Y, Mabru C, Labarrrée M, Arurault L, Tonon C, Guigue P (2010) Mechanical behaviour of black anodic films on 7175 aluminium alloy for space applications. Met Finish 108:22–27

33. Jaya Rao VVS, Kannan E, Prakash KRV (2009) Balasubramaniam: observation of two stage dislocation dynamics from nonlinear ultrasonic response during the plastic deformation of AA7175-T7351 aluminium alloy. Mater Sci Eng A 512:92–99

34. Shao G, Zhu S, Wang Y, Zhao Q (2017) An internal state variable thermodynamic model for determining the Taylor-Quinney coefficient of glassy polymers. Int J Mech Sci 126:261–269

35. Fekete B, Szekeres A (2015) Investigation on partition of plastic work converted to heat during plastic deformation for reactor steels based on inverse experimental-computational method. Eur J Mech A Solids 53:175–186. https://doi.org/10.1016/j.euromechsol.2015.05.002zaere

36. Knysh P, Korkolis YP (2015) Determination of the fraction of plastic work converted into heat in metals. Mech Mater 86:71–80

37. Maurel-Pantel A, Baquet E, Bikard J, Bouvard JL, Billon N (2015) A thermo-mechanical large deformation constitutive model for polymers based on material network description: application to a semi-crystalline polyamide 66. Int J Plast 67:102–126

38. Billon N (2012) New constitutive modelling for time-dependent mechanical behavior of polymers close to glass transition: fundamentals and experimental validation. J Appl Polym Sci 125:4390–4401

39. Benaarbia A, Chrysochoos A, Robert G (2014) Kinetics of stored and dissipated energies associated with cyclic loadings of dry polyamide 6.6 specimens. Polym Test 34:155–167

40. Zaera R, Rodríguez-Martínez JA, Rittel D (2013) On the Taylor-Quinney coefficient in dynamically phase transforming materials. Application to 304 stainless steel. Int J Plast 40:185–201. https://doi.org/10.1016/j.ijplas.2012.08.003

41. Rusinek A, Klepaczko JR (2009) Experiments on heat generated during plastic deformation and stored energy for TRIP steels. Mater Des 30(1):35–48. https://doi.org/10.1016/j.matdes.2008.04.048. Accessed 21 Sept 2022

42. Badulescu C, Grédiac M, Haddadi H, Mathias J-D, Balandraud X, Tran H-S (2011) Applying the grid method and infrared thermography to investigate plastic deformation in aluminium multicrystal. Mech Mater 43:36–53. https://doi.org/10.1016/j.mechmat.2010.11.001

43. Dulieu-Barton JM (1999) Introduction to thermoelastic stress analysis. Strain 35:35–39

44. Pitarresi G, Patterson EA (2003) A review of the general theory of thermoelastic stress analysis. J Strain Anal Eng Des 38(5):405–417. https://doi.org/10.1243/03093240360713469. Publisher: IMECHE. Accessed 2 Dec 2021

45. Lemaitre J, Chaboche J-L (1990) Mechanics of solid materials. Cambridge University Press, Cambridge. https://doi.org/10.1017/CBO9781139167970

46. Bertram A, Krawietz A (2012) On the introduction of thermoplasticity. Acta Mech 223:2257–2268

47. Jones W, March NH (1986) Theoretical solid state physics. Dover Publishing, New York.

48. Tan JC, Tsipas SA, Golosnoy IO, Curran JA, Paul S, Clyne TW (2006) A steady-state Bi-substrate technique for measurement of the thermal conductivity of ceramic coatings. Surf Coat Technol 201(3):1414–1420. https://doi.org/10.1016/j.surfcoat.2006.02.010. Accessed 26 Jan 2022

49. Kosky P, Balmer R, Keat W, Wise G (2021) Chapter 14 - Mechanical engineering. In: Kosky P, Balmer R, Keat W, Wise G (eds) Exploring Engineering (Fifth Edition). Academic Press, pp 317–340 https://doi.org/10.1016/B978-0-12-815073-3.00014-4. https://www.sciencedirect.com/science/article/pii/B9780128150733000144. Accessed 28 Jun 2022

50. ASM International (2011) Atlas of Stress-strain Curves. ASM International, Materials Park, OH. OCLC: 1131451638

51. Cheong LW, Marc F (2018) Experimental and numerical investigations into the behaviour of a 7175-T7351 aluminium alloy for aerospace gearbox housing applications at elevated temperatures. PhD thesis, University of Nottingham. http://eprints.nottingham.ac.uk/49366/. Accessed 30 Nov 2022

52. Kuneš J (2012) Thermomechanics. In: Kuneš J (ed) Dimensionless Physical Quantities in Science and Engineering. Elsevier, Oxford, pp 173–283. https://doi.org/10.1016/B978-0-12-416013-2.00005-1. https://www.sciencedirect.com/science/article/pii/B9780124160132000051. Accessed 29 Sept 2022

53. Zhang T, Guo Z-R, Yuan F-P, Zhang H-S (2018) Investigation on the plastic work-heat conversion coefficient of 7075–T651 aluminum alloy during an impact process based on infrared temperature measurement technology. Acta Mech Sin 34(2):327–333. https://doi.org/10.1007/s10409-017-0673-8. Accessed 21 Feb 2022

54. Crameri F, Shephard GE, Heron PJ (2020) The misuse of colour in science communication. Nat Commun 11(1):5444. https://doi.org/10.1038/s41467-020-19160-7